Ocean Engineering 37 (2010) 26–36

Contents lists available at ScienceDirect

Ocean Engineering

journal homepage: www.elsevier.com/locate/oceaneng

Reconstruction of Hurricane Katrina's wind fields for storm surge and wave hindcasting

Mark D. Powell [a,*], Shirley Murillo [a], Peter Dodge [a], Eric Uhlhorn [a], John Gamache [a], Vince Cardone [b], Andrew Cox [b], Sonia Otero [c], Nick Carrasco [c], Bachir Annane [c], Russell St. Fleur [c]

[a] NOAA-AOML Hurricane Research Division, Miami Florida, USA
[b] Oceanweather, Inc. Coc Cob, CO, USA
[c] Cooperative Institute for Marine and Atmospheric Studies, University of Miami, Miami, FL, USA

ARTICLE INFO

Article history:
Received 7 November 2008
Accepted 26 August 2009
Available online 4 September 2009

Keywords:
Hurricane
Katrina
Hurricane surface winds
Storm surge
Hurricane waves
Integrated kinetic energy

ABSTRACT

As the most costly US natural disaster in history, Hurricane Katrina fostered the IPET forensic study to better understand the event. All available observations from several hundred space-, land-, sea-, and aircraft-based measurement platforms were gathered and processed to a common framework for height, exposure, and averaging time, to produce a series of wind field snapshots at 3 h intervals to depict the wind structure of Katrina when in the Gulf of Mexico. The stepped-frequency microwave radiometer was calibrated against GPS sondes to establish the upper range of the instrument and then used to determine the wind field in the storm's core region in concert with airborne Doppler radar winds adjusted to the surface from near the top of the PBL (500 m). The SFMR data were used to develop a method to estimate surface winds from 3 km level reconnaissance aircraft observations, taking into consideration the observed azimuthal variation of the reduction factor. The "SFMR method" was used to adjust reconnaissance flight-level measurements to the surface in the core region when SFMR and Doppler winds were not available. A variety of coastal and inland mesonet data were employed, including portable towers deployed by Texas Tech University, University of Louisiana at Monroe, and the Florida Coastal Monitoring Program, as well as fixed mesonet stations from Louisiana State Universities Marine Consortium, University of Southern Mississippi, and Agricultural Networks from Louisiana, Mississippi, and Alabama, and the Coastal Estuarine Network of Alabama and Mississippi. Also included were land- (WSR-88D VAD and GBVTD, ASOS, Metar, LLWAS, HANDAR), space- (QuikScat, GOES cloud drift winds, WindSat), and marine- (GPS sondes, Buoys, C-MAN, ships) platforms. The wind fields serve as an analysis of record and were used to provide forcing for wave and storm surge models to produce hindcasts of water levels in the vicinity of flood control structures.

Published by Elsevier Ltd.

1. Introduction

In order to understand the performance of flood control systems during Hurricane Katrina it was essential to model the forces associated with winds, waves, and storm surge. Since the surface wind stress provides the forcing for the waves and surge, accurate wind field information is necessary to model realistic storm surge and waves. NOAA's Hurricane Research Division of the Atlantic Oceanographic and Meteorological Laboratories participated in the Interagency Performance Evaluation Task Force (IPET) with the responsibility of reconstructing the Katrina's wind field. Oceanweather participated by using the IOKA system to blend the H*Wind fields with larger scale observations and then interpolate the gridded fields to times and resolutions required by the wave and storm surge models.

Observations from a large number of air-, land-, sea-, and space-based measurement platforms were obtained, standardized, evaluated and analyzed in order to provide a mesoscale analysis of record to serve as the best available depiction of Katrina's wind field for use in wave and surge modeling. Wind field analysis was first conducted in real-time as part of NOAA's research to understand and predict hurricane impacts. A limitation of the real-time analyses is that they were based on data collected 4–6 h before the analysis time. Months later, the analyses were improved with additional data that were not available in real-time. The post-storm analyses are more accurate due to the availability of more observations with more detailed standardization processing and quality control. The post-storm analyses are more representative of storm conditions since they use all observations within 3 h of the analysis time. The

* Corresponding author.
E-mail address: Mark.Powell@noaa.gov (M.D. Powell).

0029-8018/$ - see front matter Published by Elsevier Ltd.
doi:10.1016/j.oceaneng.2009.08.014

post-storm analyses are the basis for winds used by the storm surge and wave model components of the IPET study. This paper will describe the hurricane wind analysis system in Section 2, observation data sources and standardization methods in Section 3, the evolution of Katrina's wind field in Section 4, and the blending of gridded analysis data with larger scale analysis information and interpolation to more frequent time intervals for support of wave and surge models in Section 5.

2. The NOAA–HRD hurricane wind analysis system (H*Wind)

The prototype of the NOAA–HRD hurricane wind analysis system (H*Wind, Powell and Houston, 1996) was used to reconstruct the wind field of Hurricane Andrew's South Florida landfall. Later interactive features were added and a distributed architecture was implemented as described in Powell et al. (1998). The current version of H*Wind provides to forecasters guidance on the magnitude and extent of the tropical storm and hurricane force winds. Real-time analyses are conducted on a 6 h cycle designed to deliver products about 1.5 h before forecasts and advisories are issued by the National Hurricane Center (NHC). During tropical cyclone warnings, the analysis cycle is increased to a 3 h frequency to match the enhanced operational cycle. It is important to recognize that H*Wind fields are not official products of NHC. H*Wind is a research application and provides an estimate of the wind field based on all available observations over a several-hour "time window". All observations are composited as a range and bearing relative to the location of the storm at the time of the observation. This time-to-space compositing technique was originally developed by Cline (1920). H*Wind allows the analyst to plot all observations either where they were actually located (synoptic or earth-relative) or according to their location relative to the storm. This simple time-to-space compositing for storm-relative analysis has the advantage of filling in data coverage gaps. The analysis is considered representative of storm conditions at the center time of a several-hour period. The analyst faces a choice of minimizing the time window at the expense of data coverage or maximizing the data coverage at the expense of representativeness. Usually a 4–6 h time window will contain sufficient observations and data coverage for an analysis. H*Wind analyses described here use a 6 h time window containing 3 h of observations on either side of the center time. The analysis is constrained to match the maximum observed surface wind speed over the 6 h period. Since it takes a reconnaissance aircraft about 6 h to sample the wind field of the hurricane, it is difficult to resolve the timing of peak intensity to better than 3 h about any analysis time.

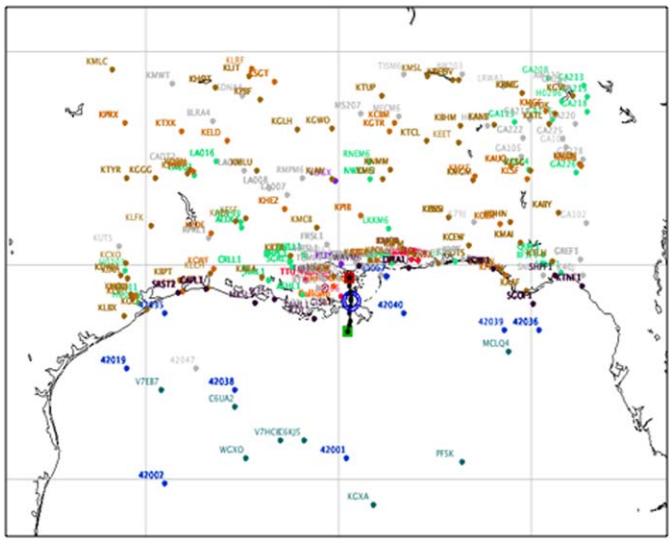

Fig. 1. Observation platform locations for 1200 UTC 29 August analysis. Orange are FCMP, Red are TTU, and USA, Brown are FAA, METAR, and ASOS, Green are MADIS, Dark Blue is NDBC moored buoy, Aqua are ships, CMAN are black, VAD are purple, and Gray are observations flagged during quality control. Latitude lines are for 25.3°, 30.3°, and 35.3°N and longitude lines are 94.9°, 89.9°, and 84.9°W. (For interpretation of the references to color in this figure legend, the reader is referred to the web version of this article.)

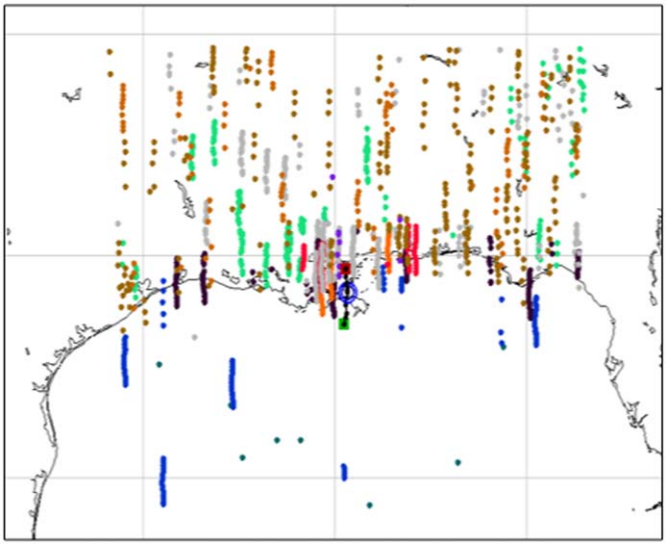

Fig. 2. As in Fig. 1 but in storm relative coordinates over the time period of 0900–1500 on 29 August 2005.

3. H*Wind data sources and standardization

The Katrina wind field reconstruction constituted the most comprehensive hurricane wind assessment yet attempted. This effort required obtaining observations from a wide variety of land-, sea-, space-, and air-based wind measurement platforms. Each observing system has specific sensor characteristics, measurement heights, upstream fetches, and averaging times. H*Wind uses standardization methods (Powell et al., 1996) to process all observations to a common framework for height (10 m), exposure (marine and open exposure), and averaging time (maximum 1 min wind speed). An example of the Katrina wind analysis data coverage for the 1200 UTC 29 August 2005 Katrina wind analyses is shown in Fig. 1 which depicts the actual (earth-relative) locations for marine, coastal, and inland observing platforms (for clarity, satellite, aircraft, and Doppler radar observations are not shown). H*Wind takes advantage of the changing storm-relative locations of these stations during the 0900–1500 UTC time period to improve data coverage and help fill-in data gaps, resulting in the storm-relative data distribution shown in Fig. 2. Essentially, one station is transformed into a line of observations parallel to the storm track. The various observing systems and standardization procedures are discussed below:

3.1. Marine and coastal observing platforms

Table 1 provides an overview of various marine, coastal, and inland and observing systems. Among the marine and coastal

stations are NOAA National Data Buoy Center and University of Southern Mississippi moored buoys, coastal platforms from the Coastal-Automated Marine Network (C-MAN), National Ocean Service (NOS), Louisiana Universities Marine Consortium (LUMCON), the Louisiana State University (LSU) Wave-Current-Surge Information System for Coastal Louisiana (WAVECIS), the Gulf of Mexico Ocean Observing System-Regional Association (GCOOS-RA), and the Weeks Bay, AL Network of the National Estuarine Research Reserve System.

Marine observations were standardized as described in Powell et al. (1996), using the Liu surface layer model (Liu et al., 1979) to compute the 10 min mean wind at 10 m level. The only change to the Liu model was to use the Large and Pond drag coefficient relationship for wind speeds $<34\,m\,s^{-1}$ and hold the drag coefficient constant at 2×10^{-3} for winds above hurricane force consistent with observations from GPS sondes in hurricanes (Powell et al., 2003). The maximum 1 min sustained wind speed was then computed by multiplying the mean marine surface wind speed by a gust factor (see below).

Table 1
Coastal, marine, and inland weather networks.

Network	Number of stations	Anemometer heights (m)	Averaging time (min)
FCMP	5	10	Peak 1/15 min
TTU	3	10	Peak 1/10 min
ULM	1	2	Peak 1/10 min
LAIS	25	10	10
ASOS	60	7–10	2
METAR	22	7–11	2
LLWAS	3	9–16	2
EOC's	3	7–16	1, Peak 3 s gust
C-MAN	4	12–30	10
MADIS	28	Variable	Variable
LUMCON	3	10–13	1–2
Wave CIS	5	5–40	10
GCOOS-RA	1	5	10
NWS New Orleans	1	9–16	10
NOS	7	6–10	6–10
USA	4	4–11	10
DOD	3	10	2
NDBC Moored Buoys	9	5–10	10
National Estuarine Research Reserve System (Weeks Bay, AL)	2	4–11	10

3.2. Land-based observation platforms

Observing platforms over land (Table 2) include portable mesonet stations deployed by the Florida Coastal Monitoring Program (FCMP, 5 towers), Texas Tech University (TTU, 3 towers), University of Louisiana at Monroe (ULM, 1 tower), Low-Level Wind Shear Alert System network surrounding New Orleans (3 stations), a New Orleans Weather Forecast Office automated station on the Lake Ponchartrain Causeway, an agricultural network of 25 stations operated by Louisiana, Mississippi, and Alabama as part of the Louisiana Agriclimatic Information System (LAIS), and observations logged by Emergency Operations Centers at NASA Michoud, Pearl River, and Pascagoula. Conventional weather stations included the Automated Surface Observing System (ASOS, 60 stations), Aviation weather stations (METAR, 22 stations), and 28 miscellaneous stations from the Meteorological Assimilation Data Ingest System (MADIS).

Winds measured by land platforms (including coastal platforms for some offshore wind directions) are influenced by friction associated with upstream terrain features. In these cases standardization requires knowledge of the upstream terrain roughness. The FCMP and TTU observations contained estimates of surface roughness determined from measurements of turbulence intensity. For the remaining stations, roughness (Z_o) was estimated for each wind direction octant with upstream influence based on photographic documentation (Powell et al., 2004) or using aerial photographs and satellite imagery available on the web by applications such as Google Earth. Roughness estimates were subjective, based on experience guided by qualitative descriptions such as Weiringa (1992). H*Wind provides an interface to allow the scientist to edit the roughness table and zero-plane displacement heights and immediately compare the updated wind value to neighboring stations. H*Wind provides a tool to export data for plotting in Google Earth so the scientist can visualize roughness influences on the flow.

The H*Wind objective analysis requires all observations to conform to a marine exposure. For land stations, the median upstream octant station roughness estimated from aerial and site

Table 2
Selected mesonet and supplemental coastal and inland observing platforms.

Station	Lat (deg)	Lon (deg)	Anemometer height	Sampling
FCMP Stennis T0	30.38	89.455	10	Max 1 min every 15 min
FCMP Belle Chase T1	29.825	90.03	10	Max 1 min every 15 min
FCMP Galliano T2	29.444	90.263	10	Max 1 min every 15 min
FCMP Pascagoula T3	30.472	88.531	10	Max 1 min every 15 min
FCMP Gulfport T5	30.551	89.147	10	Max 1 min every 15 min
TTU Slidell SBC Clear	30.3422	89.822	10	Max 1 min every 10 min
TTU Stennis SBC White	30.3742	89.4508	10	Max 1 min every 10 min
TTU Vacherie	29.968	90.743	10	Max 1 min every 10 min
LLWAS #2	30.006	90.246	9.14	
LLWAS #8	29.982	90.265	14	
LLWAS #9	29.999	90.289	16.16	
Buras data	29.34	89.533	2.5	10 min consecutive
Lake Ponchartrain Cswy.	30.09	90.08	16.46	
NASA Michaud EOC	30.02556	89.91462	12.2	Max 1 min
LA-MS-AL AgNet Agricola	30.81655	88.52051	10	3 s continuous record
MS-AL Weeks Bay	30.4148	87.826	4	
MS-AL Middle Bay	30.433	88.02	11.3	
USM Buoy 42067				10 min mean every 30 min
Jackson County EOC, Pascagoula			17	Peak 3 s gust
Poplarville Pearl Riv. Cty EOC	30.8	89.5	7.6	Peak 3 s gust

photography was approximately open (0.05 m) with about 25% of the octant station values >0.1 m and 10% >0.25 m. Observations were first converted to a wind speed at a level within the boundary layer ($\sim$250 m) where winds are assumed to be equivalent for different terrains under neutral stability using Eq. (1), and then estimated for open terrain using Eq. (2).

Using the neutral stability logarithmic wind profile law and the ratio of the wind speed at 250 m (U_{250}) to the wind speed (U_{za}) at anemometer height (Z_a),

$$U_{250} = U_{za}\frac{Ln((250-D)/Z_o)}{Ln((Z_a-D)/Z_o)} \quad (1)$$

where D is the zero-plane displacement height. In practice, D was rarely used unless the exposure for a site was extremely poor. The 250 m wind is then used to estimate the 10 m level mean wind speed (U_{open}) for open terrain (Z_o=0.03 m),

$$U_{\text{open}} = U_{250}\frac{Ln(10/.03)}{Ln(250/.03)} \quad (2)$$

The open terrain mean winds were increased 17% to convert to a marine exposure for use in the analysis, consistent with Vickery et al. (2009). Vickery et al. (2009, Fig. 12), using a 600 m boundary layer height and 20 km fetch, found a $\sim$0.83 ratio of the fully transitioned mean flow over open terrain to that over the open ocean, compared to 21% and 19% increase from open to marine exposure for ESDU (1984) and Simiu and Scanlan (1996), respectively.

The maximum 1 min sustained wind speed over the time period of the mean wind (usually 10 min) is then computed,

$$U_{1\text{marine}} = U_{\text{marine}} * G_{\text{m60,600}} \quad (3)$$

where $G_{\text{m60,600}}$ is the marine exposure gust factor based on the method described by Vickery and Skerlj (2005).

For $U_{\text{marine}} < 34\ \text{m s}^{-1}$, the gust factor depends on the mean wind speed:

$$G_{\text{m60,600}} = 1.069 + 1.51\times10^{-3}U_{\text{marine}} \quad (4)$$

As winds increase $>34\ \text{m s}^{-1}$, the gust factor tends to level off.

$$G_{\text{m60,600}} = 1.094 \quad (5)$$

The marine-adjusted winds were then compared to actual marine observations (e.g. GPS sondes, buoys, SFMR observations, etc.) using H*Wind's graphical interactive quality control (QC) tools. Marine-adjusted land observations inconsistent with neighboring marine counterparts were "flagged" (removed from consideration). The nearest neighbor QC process ensures that the analysis is consistent with marine observations in coastal, offshore, and lake locations. Once the marine wind field analysis is completed, portions of the wind field over land locations are converted back to open terrain, as depicted in the analysis graphics described later in the paper, matching the original open terrain adjusted values.

3.3. Land-based and airborne radar

Four radar-based wind measurement methods were used to estimate winds near the top of the boundary layer. An advantage of Doppler radar techniques is the ability to determine winds over a relatively large area, resolving the azimuthal variation in the maximum wind.

(1) Observations from the Slidell and Mobile WSR-88D Doppler radars were used to generate dual-Doppler analysis at for the 500 and 1000 m levels.
(2) The ground based velocity track display (GBVTD) technique Lee et al., 1999) was used to generate wind fields at the 500 and 1500 m levels on 1010 UTC on 29 August (Fig. 3). An advantage of the GBVTD is that only one radar is needed to produce a wind field.
(3) The tail Doppler radars aboard the NOAA P3 aircraft scan in a fore-aft sampling pattern which enables a dual-Doppler

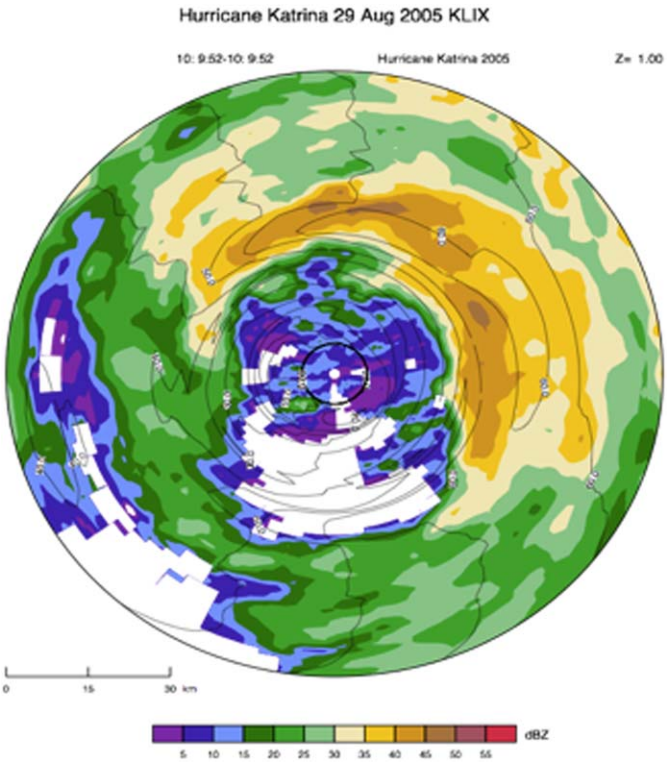

Fig. 3. GBVTD wind field analysis for the 1.0 km level from the Slidell WSR-88D Doppler radar for 1010 UTC on 29 August.

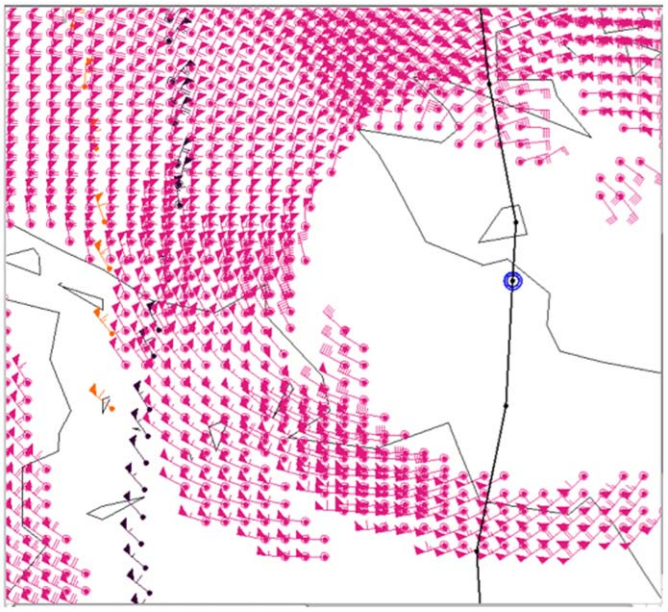

Fig. 4. H*Wind screen grab of NOAA 43 Airborne Doppler radar winds adjusted to the surface (red) for 1232 UTC. Also plotted are 10 min observations from Grand Isle C-MAN station (GDIL1) in black (1000–1224 UTC) and Belle Chase FCMP tower in orange (1218–1351 UTC). (For interpretation of the references to color in this figure legend, the reader is referred to the web version of this article.)

analysis technique (Gamache et al., 1995) to determine winds at the 500 and 1000 m levels (e.g. 1232 UTC, Fig. 4).

(4) A fourth method involved evaluation of winds close to the land-based radar sites using the velocity azimuth display (VAD) technique. This method generates a vertical profile of the horizontal wind based on data from 2–9 km from the radar.

For each method, winds at these levels were then adjusted to the surface empirically, based on their comparison to marine observations in the same storm-relative location. The resulting winds were then evaluated against observations from other platforms to see how well they fit with in-situ surface measurements. In locations where they did not agree, the surface measurements were given precedence and the radar observations were "flagged" so they would not be used in the final objective analysis.

3.4. Aircraft reconnaissance observations

Flight-level observations were available from the NOAA P3 and Air Force Reserves C-130 aircraft, typically at the 70 hPa level near 3 km altitude. The NOAA P3 aircraft also carried the stepped-frequency microwave radiometer (SFMR), which measures wind speed based on the microwave emission from sea foam at five different frequencies. The SFMR resolves the radial location of the surface wind maximum with far greater accuracy than GPS sondes which can easily miss the location of maximum winds. A detailed calibration–validation of the SFMR was conducted in 2004 and 2005 and involved comparisons to over 400 GPS sondes (see Uhlhorn and Black, 2003; Uhlhorn et al., 2007). The SFMR is considered to be a high-accuracy marine platform comparable to 10 m discus buoys and GPS sondes.

Comparisons between flight-level and SFMR maximum winds on each radial flight leg were used to develop specific surface adjustment methods for flight-level observations on each day for 27, 28, and 29 August. These methods (Fig. 5) determined the radius and aziumuth of the maximum surface wind relative to the maximum flight-level wind and also specified the radial variation of the winds. The radius of surface wind maximum is typically located at about 85% of the flight-level radius of maximum wind Powell et al. (2009). The ratio of the maximum surface wind to the maximum flight-level wind (the slant reduction factor) varied between 28 August and landfall with higher values on the 28th. A vertical reduction factor was determined on each day for the variation of reduction factor with radius outside the vicinity of the eyewall. The methods were applied to the Air Force flight-level winds when the NOAA SFMR data were not available.

GPS sondes are routinely launched by both NOAA and Air Force reconnaissance aircraft. Two surface wind estimates are provided. A surface wind is computed based on the 0.5 s sampled motion of the sonde near 10 m (see Hock and Franklin, 1999). In extreme winds, turbulence below 200 m makes it difficult for the GPS sonde to "find" enough satellites to do the wind computation. A GPS sonde surface measurement (even with 10 s filtering) shows high variability representative of the flow features it happens to be falling through, and the semi-Lagrangian measurement is difficult to relate to a conventional anemometer averaging time. An alternative surface wind estimate relating the GPS sonde surface wind to the mean wind over the lowest 150 m (WL150) was developed by Franklin et al. (2003). The WL150-determined surface wind tends to be less variable than the surface wind and is considered a high quality observation during the quality control process. During landfall, SFMR and GPS sonde observations were available over Lake Ponchartrain and just offshore Mississippi Sound.

3.5. Satellite observations

Wind measurements were available from the Sea Winds scatterometer aboard QuikScat (Quilfen et al., 2007) and from

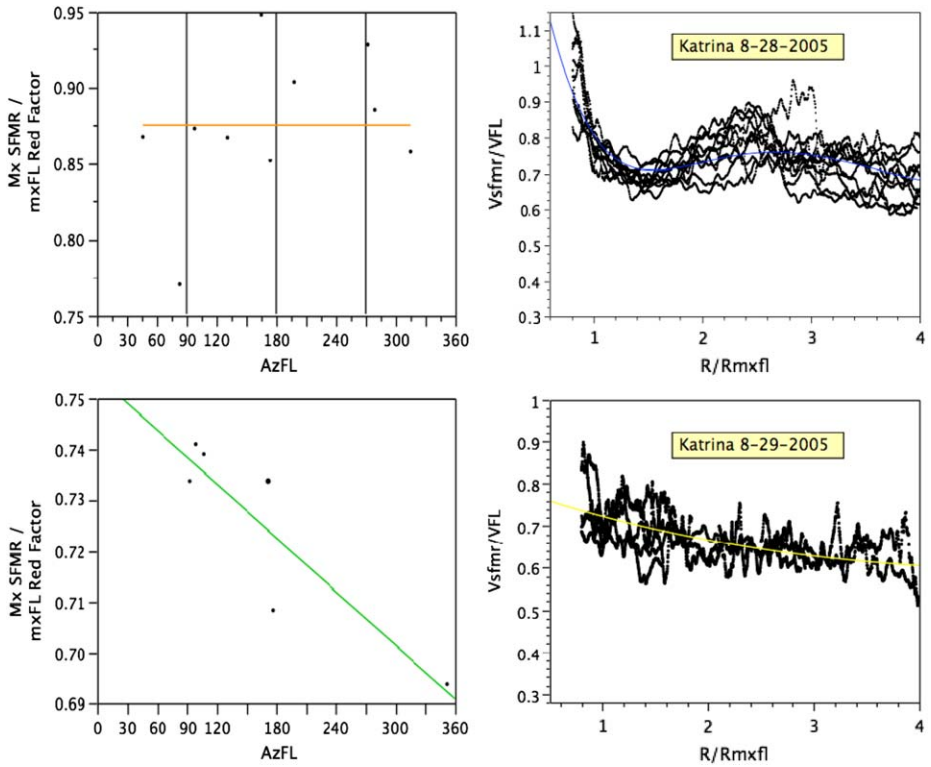

Fig. 5. Azimuthal variation (left) of the slant reduction factor in Katrina on 28 August, 2005 (top) and 29 August (bottom). Right panels show variation in the reduction factor as a function radius scaled by the radius of the flight-level maximum wind speed.

tracking visible GOES imagery for cloud motions at low levels. The QuikScat winds sometimes have direction errors associated with poor first guesses but tend to be contaminated by rain and cloud at winds over about 30 m s^{-1} but otherwise help fill-in areas missed by the aircraft and help to identify the extent of the damaging wind field. When standardizing QuikScat winds for H*Wind, we first determine a time scale for the wind measurement attributed to a grid cell by dividing the grid cell dimension by the wind speed. A gust factor is then applied (Powell et al., 1996) to estimate the highest 1 min wind over the time scale attributed to the grid cell. Cloud drift winds were computed by the University of Wisconsin-NOAA Cooperative Institute for Meteorological Satellite Studies (CIMSS) at pressure levels below 70.0 hPa. Cloud drift winds were adjusted to the surface following the method of Dunion et al. (2002).

4. The evolution of Katrina's wind field

Time series of minimum sea-level pressure (Fig. 7) and intensity (Fig. 6) show Katrina's evolution from a strong tropical storm on entry into the Gulf of Mexico (0000 UTC, 26 August) to maximum intensity (1200–1800 UTC 28 August), to landfalls in Louisiana and Mississippi (1200, 1500 UTC, 29 August), and finally to a decaying system (1200 30 August). Intensity is defined by the maximum 1 min sustained surface wind anywhere in the storm at a particular time. Intensities in Fig. 6 are based on H*Wind analyses. The change in sea-level central surface pressure on Fig. 7 provides an alternate assessment of intensity change and is sampled more frequently than the maximum wind since over a 6 h period the aircraft may sample the location (azimuth on a radial flight leg) of maximum winds only once but sample the center of the eye several times. Based on pressure, the period of Katrina's most rapid intensification was from 0600 to 0900 on 28 August and the period with the most rapid weakening was 1500–1800 29 August H*Wind analyses for 0900 UTC for 28 August and the 1800 UTC 29 August are based on time periods with the most rapid changes, so the maximum wind estimates are not necessarily at the analysis time but capture the peak measured intensity within 3 h of that time.

As Katrina emerged from the Florida peninsula into the Gulf of Mexico, the intensity ramped up slowly but steadily from about 72 kts (35 m s^{-1}) at 0900 UTC 26 August to 87 kts (48 m s^{-1}) at 2100 UTC 27 August, while the pressure fell from 98.5 to 95.0 hPa.

During this time period Katrina's ability to maintain healthy convection effectively shielded it from dissipative effects of wind shear (McTaggart-Cowan et al., 2007) and the extent of hurricane force and 50 kt wind doubled. From 2100 UTC 27 August to 1200 UTC on 28 August (Fig. 8), a period of rapid intensity change commenced with the passage of Katrina over relatively deep layers of warm water associated with the Gulf of Mexico Loop Current and a warm-core ring feature to the west (Fig. 9). Upwelling and ocean mixing associated with strong winds in the vicinity of Katrina's core transported relatively warm water to the surface, effectively removing a brake to intensification (in the absence of these high ocean heat content features, a hurricane would normally transport cooler subsurface water to the surface, inhibiting surface enthalpy fluxes). While passing over these ocean features, Katrina reached her maximum intensity of 139 kts (72 m s^{-1}) while pressure fell to 90.5 hPa. During the intensification period the radius of maximum surface wind (Rmax) contracted from 50 to 25 km, and the extent of hurricane, 50 kt, and tropical storm-force winds continued to

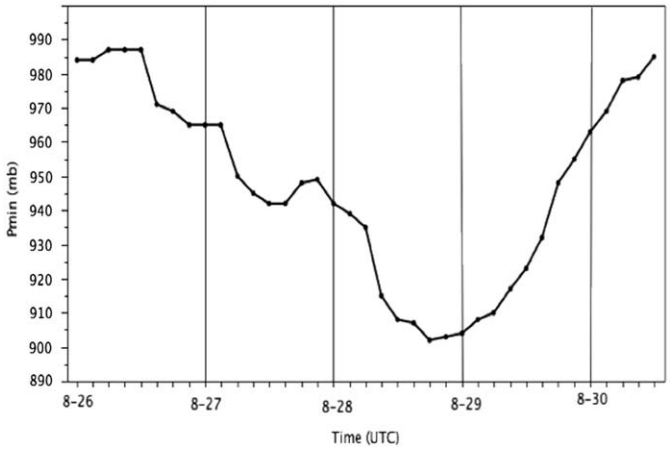

Fig. 6. Time series of 3 h maximum sustained surface wind speed.

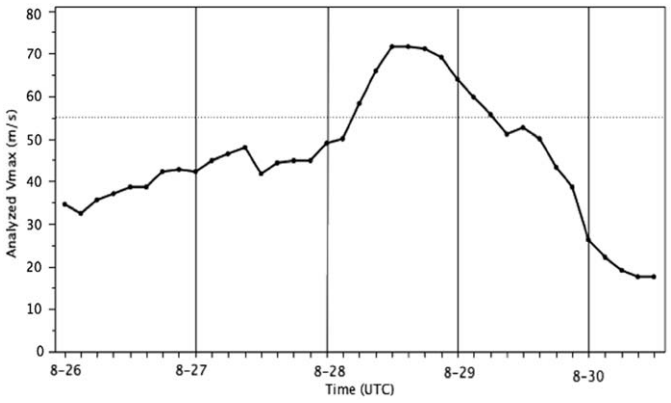

Fig. 7. Time series of 3 h central sea-level surface pressure.

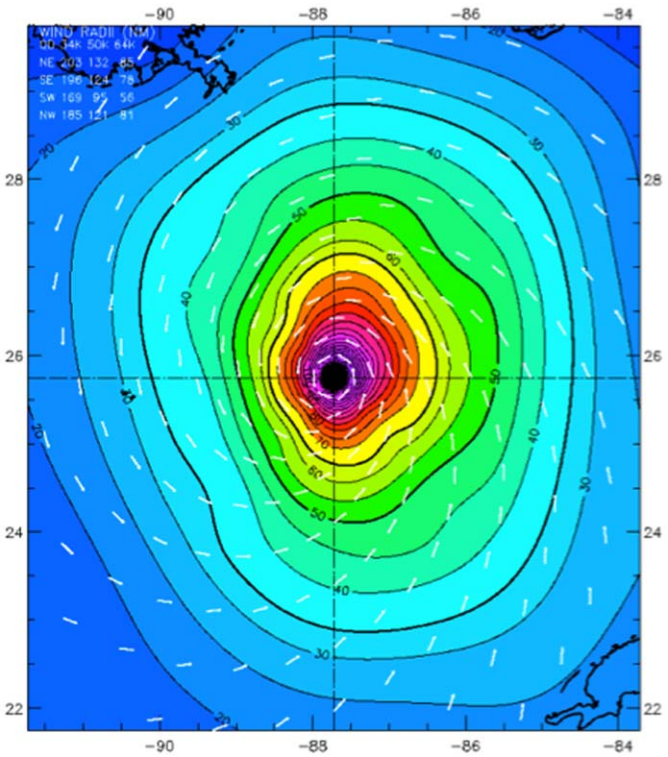

Fig. 8. H*Wind analysis for Katrina's entrance into the Gulf of Mexico at 1200 UTC, 28 August 2005. Wind speed contours in kts. Box in upper left shows radial extent (nm) of hurricane, 50 kt, and tropical storm strength winds in each quadrant.

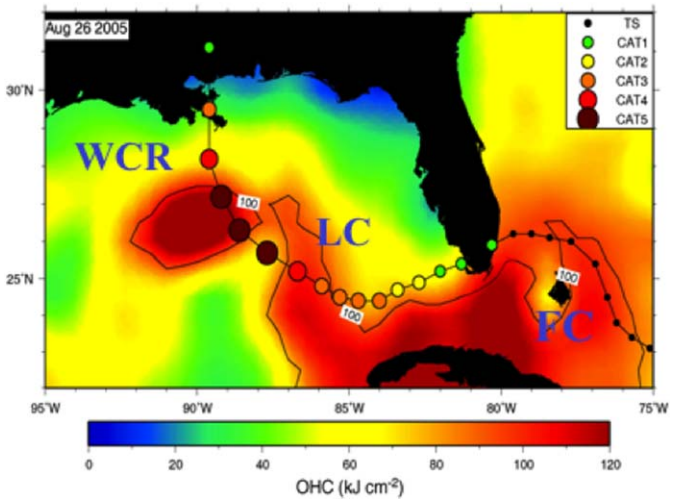

Fig. 9. Pre-Katrina ocean heat content (from Shay, in press) depicting Katrina's track and Saffir–Simpson scale relative to positions of the Loop Current (LC), Florida Current (FC), and warm core ring (WCR). Ocean heat content based on altimetry data from Jason-1, Geosat Follow-On, and Envisat data.

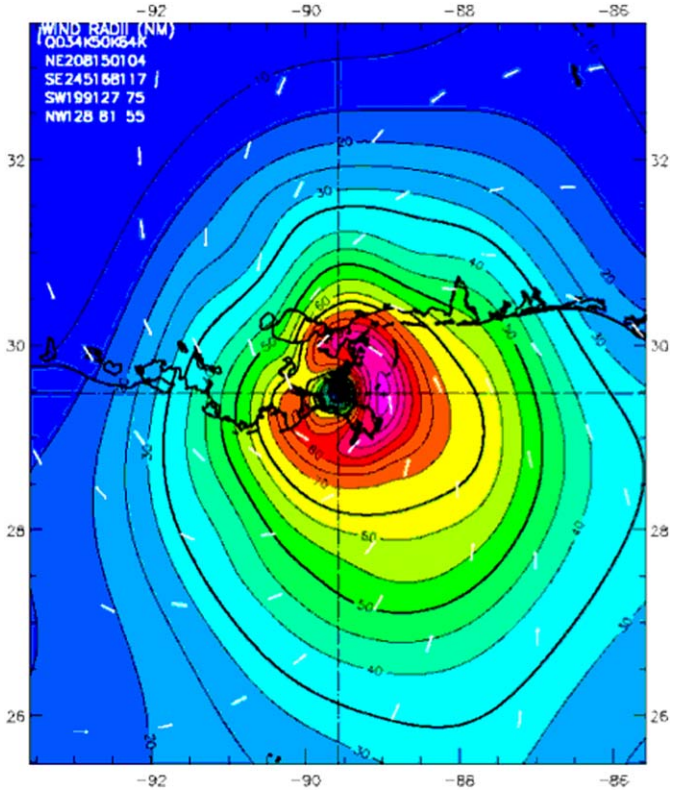

Fig. 10. As in Fig. 8 but for landfall at 1200 UTC, 29 August 2005.

increase. There was no clear indication of an eyewall replacement cycle (Willoughby et al., 1982; Houze, 2007), rather a "superintensity" process may have been acting, through which the eyewall gains fuel from mixing with the eye (McTaggart-Cowan et al., 2007; Persing and Montgomery, 2003). For the next several hours Katrina's wind field maintained this size and intensity with the central pressure remaining below 91.0 hPa and the extent of hurricane force, 50 kt, and tropical storm-force winds at 130, 220, and 370 km, respectively through 2100 on 28 August.

During the next 15 h while Katrina approached land, the pressure rose while Katrina moved over Gulf of Mexico shelf waters containing relatively low ocean heat content. As Katrina's center was making landfall in Louisiana at 1200 UTC on 29 August (Fig. 10), a series of outer rainbands formed which acted effectively as an outer eyewall (Fig. 11). The outer eyewall (60 km radius) became predominant and contained winds slightly higher than those in the inner eyewall. The outer eyewall feature was not particularly well defined on radar, nor by the flight-level winds on the reconnaissance aircraft. While the pressure rose and the winds in the eyewall decreased to 102 kts ($53\,m\,s^{-1}$) as a consequence of angular momentum conservation, the radius of maximum wind increased, and the extent of hurricane-, 50 kt, and tropical storm-force winds increased to 200, 300, and 400 km.

Radar reflectivity images (Fig. 11) from three different radars (NOAA-43 research aircraft, Slidell, and Mobile National Weather Service WSR-88D) show conflicting depictions of secondary outer eyewalls brightness temperatures compared to the Morphed Integrated Microwave Imagery (MIMIC) 85–92 GHz signal of low earth orbiting satellites (Wimmers and Velden, 2007). The radars tend to agree on major features (inner eyewall and a series of spiral bands to the north and northeast of the storm center) while the MIMIC product suggests a coherent outer eyewall adjacent to a moat region with lower brightness temperatures. Outer eyewall features depicted in radar and MIMIC often show large changes in reflectivity and brightness temperature between the outer band and "moat" region between the inner and outer eyewall. These large magnitudes in the outer eyewall often produce an interpretation and expectation of dramatic outer wind maxima. In-situ data show a much more subtle signal, typically only $1–2\,m\,s^{-1}$ above winds in the vicinity. Examination of radial passes of flight-level and SFMR surface wind measurements indicated that surface outer maxima were not always present when flight-level maxima were evident, and vice versa. Sometimes the surface maximum was associated with the inner eyewall while the flight-level wind maximum was in the outer eyewall, and vice versa. Furthermore, over a 4–6 h period, as the outer bands continually generated and propagated, the location of the maxima would shift such that the outer maximum could be located at different radii and azimuths from pass to pass, consistent with the radar depictions of multiple outer rainbands. When conducting an objective analysis of such data, the subtle outer maxima tend to be smoothed out leaving the inner maximum, or the outer maxima are slightly greater than the inner maximum and the radius of maximum wind shifts accordingly.

At 1500 UTC, Katrina made a second landfall on the Mississippi coast (Fig. 12) after the center of circulation crossed Plaquemines Parish to Mississippi Sound. Land interaction led to a decrease in the intensity of the storm to $50\,m\,s^{-1}$ and the size of the wind field and by 1500 UTC (Category three on the Saffir–Simpson (SS) scale). By 0600 the following day Katrina had had moved 200 km inland and decayed to a tropical storm.

As discussed in Powell and Reinhold (2007), the pre-landfall expansion of Katrina's wind field allowed the integrated kinetic energy of the wind field (the squares of all grid cell winds exceeding tropical storm-force are multiplied by the volume of the grid cell over a 1 m depth centered at 10 m, and then summed) to remain near constant at about 120 TJ from the time of peak intensity (1200 UTC on the 28th of August) until landfall (Fig. 13). Therefore, Katrina at landfall maintained a Category 5 rating on the Powell–Reinhold storm surge destructive potential scale, despite being rated Category 3 on the SS scale. In comparison, Powell and Reinhold (2007) found that Hurricane Camille of 1969, although a Category 5 storm on the SS scale, maintained a much smaller wind field at landfall with nearly half the integrated kinetic energy of Katrina.

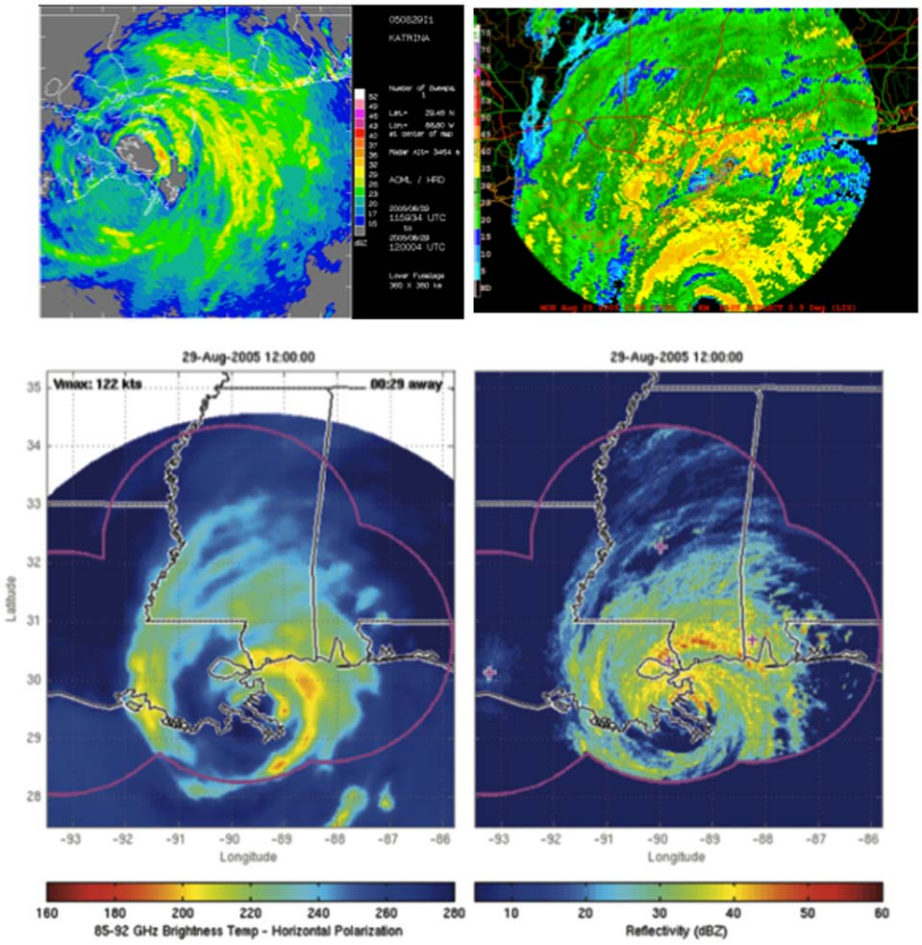

Fig. 11. Radar images of Katrina at landfall 1200 UTC 29 August 2005. Top left from NOAA 43 P3 lower fuselage radar, top right from Mobile WSR 88D, Lower right from Slidell WSR-88D, lower left brightness temperature signal from morphing 85–92 GHz return from lower earth orbiting satellites (lower panels Fig. 4 from Wimmers and Velden, 2007).

5. Conversion of sustained winds to mean winds for surge and wave forcing

The reanalyzed H*Wind snapshots of peak sustained wind speed and direction at 10 m elevation provide winds at 3 h intervals over a storm-centered domain of approximately 1000 km square on a rectangular grid of spacing that varies from 1 to 1.5 km between 0000 UTC 26 August and 0300 UTC 29 August and approximately 5 km over the period 0600 UTC 29 August to 1200 UTC 30 August. The procedure followed to transform these 3 h snapshots into a time and space continuous wind field over the entire domain of the hydrodynamic and wave models applied to Katrina is described in this section. The wind field target domain and time step required extends to the whole of the Gulf of Mexico as follows:

Basin grid spacing :	.1°	Basin grid domain :	18−30.8°N 98−80°N
Regional grid spacing :	.025°	Regionalgriddomain :	28.5−30.8°N 91−87°W
Wind field time interval :	15 min		

The first step is to interpolate all H*Wind snapshots to a working grid of uniform spacing of .02° in latitude and longitude (~2.2 km spacing) using bilinear transformation on U and V wind components to interpolate wind direction, and on wind speed directly for scalar speed. To allow additional spin-up for the ocean response models, the wind fields were actually generated beginning at 1800 UTC 24 August. An additional nine H*Wind snapshots as produced in real-time were available to cover this additional spin-up period.

The H*Wind wind speeds are transformed from peak sustained wind speed (which is essentially a stochastic variable) into equivalent 30 min average wind speeds using the factor 0.81 which is 1/1.235, where 1.235 is a slightly lowered estimate of an adopted gust factor from peak 1 min wind speed to 30 min average of 1.24 (Black, 1994). The slight reduction from 1.24 to 1.235 is based experience to compensate for a small energy loss due to the grid transformation. In more recent (i.e. post IPET) hurricane wind field reconstructions we have adopted the combination of spline interpolation and the wind speed dependent gust model of ESDU (1982) which trends at hurricane wind speeds towards a slightly lower gust ratio of 1.215.

The next step is to kinematically analyze wind fields on the periphery of the domain of H*Wind in order to fill the target domain noted above. This is accomplished with an analyst-directed interactive kinematic objective analysis (IOKA) system (Cox et al., 1995) whose workstation (WindWorkStation or WWS) displays all conventional wind data from NDBC buoys, C-MAN stations, transient ships, offshore platforms, QuikSCAT and NOAA NWP model surface wind analyses. Before display, the 10 min average winds sampled by the NOAA buoys are bin-averaged to 30 min, land stations with known exposure are brought to marine exposure, and all other data sets are brought in as is. In order to blend the outer domain wind fields into H*Wind it is only necessary to display the H*Wind field on WWS sub-sampled to about half the WWS grid of 0.5°. Fig. 14 shows an example of the WWS display at 1200 28 August 2005 (see the corresponding

H*Wind snapshot in Fig. 8). The objective analysis component of IOKA solved on a grid of 0.1° spacing. The kinematic analysis is carried out every 3 h through either hand drawn or tablet streamline–isotach analyses drawn in such a way as to ensure a smooth transition from the peripheral domain into the domain of the H*Wind fields. This step allows the final wind fields to incorporate effects on the wind field of outer rainbands, near coastal wind field deformations and other variability not captured in background NWP winds. The winds from the NDBC buoys are actively assimilated as part of the IOKA process.

The IOKA winds and the original H*Wind snapshots are then each linearly interpolated to the target time step. The H*Wind snapshots are storm-centered and interpolated in a moving coordinate system always positioned with respect to the reference storm track, which in the case of Katrina is HRD's reanalyzed track. To ensure that IOKA has not unduly degraded the H*Wind fields, within a distance of 0.5 the effective radial domain (as defined by the area covered by the original H*Wind solution) of the H*Wind fields, the interpolated snapshots are directly overlaid onto the target grid winds. Between 0.5 and 0.8 of the effective radius IOKA is applied (at the 15 min time interval) to blend H*Wind into the peripheral wind field analysis domain. Outside 0.8 of the effective radius the wind fields is entirely determined by the interpolated 3 h IOKA analyses.

The effectiveness of the spatial blending is shown in Fig. 15 (for the same time as Fig. 14). The envelope of the maximum wind speeds (30 min average) over the Gulf of Mexico is shown in Fig. 16. This figure shows the continuous evolution of the inner core maximum wind speed including some variability as Katrina moved west of the Florida coast associated with eyewall structural changes and some broadening of the wind field as the inner core

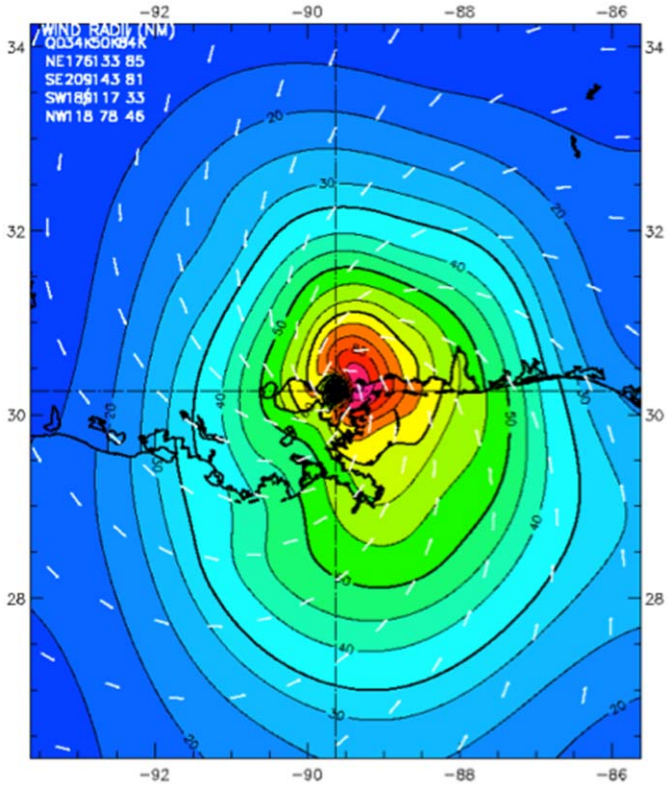

Fig. 12. As in Fig. 8 but for 1500 UTC, 29 August 2005.

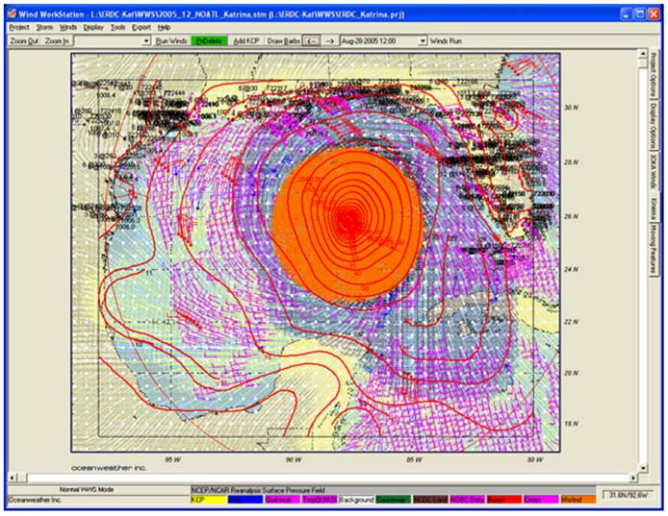

Fig. 14. WWS display valid for 28 August 2005 at 12:00 GMT showing H*Wind storm snapshot (orange) with available NWP and measured wind observations (various colors). (For interpretation of the references to color in this figure legend, the reader is referred to the web version of this article.)

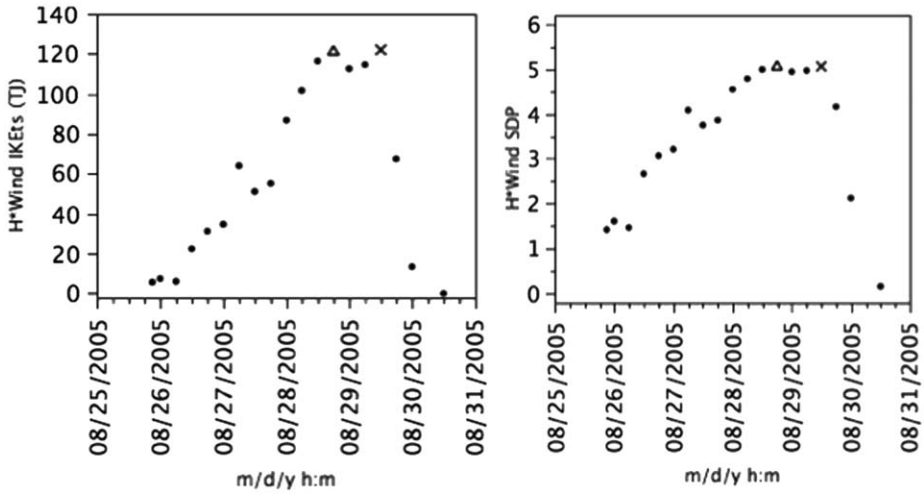

Fig. 13. Time series of integrated kinetic energy (left) and Storm surge and wave destructive potential (SDP, right) for Katrina's path in the Gulf of Mexico through landfall.

peak wind speed decreased markedly during the 24 h before landfall.

Finally, wind velocity time series and statistics of the differences between the final analyzed wind fields and the buoy measurements are provided in Table 3. The buoy measurements represent 30 min averages. The 10 m discus buoys (42001, 42003) have anemometers at 10 m elevation while the 3 m discus buoys (42007, 42040 and 42067) have anemometers at 4 or 5 m elevation (buoy 42067 is a NDBC type 3 m discus buoy maintained by the University of Southern Mississippi). These wind speeds are adjusted to 10 m elevation and equivalent neutral stratification using a surface layer wind profile of (Cardone et al., 1996). Wind speeds from the standard anemometers on the 3 m discus buoys may be biased low in extreme sea states (e.g. Howden et al., 2008) but no attempt was made to adjust the buoy measurements of wind speed for possible bias. It should be emphasized that the buoy data have been utilized in the production of both the H*Wind snapshots and the final blended IOKA wind fields on the target grids, so the good agreement between the analyses and the measurements serve more to attest to the quality of the final wind fields rather than the skill in algorithms that underlie H*Wind and/or IOKA to diagnose cyclone surface winds in the absence of in-situ measurements.

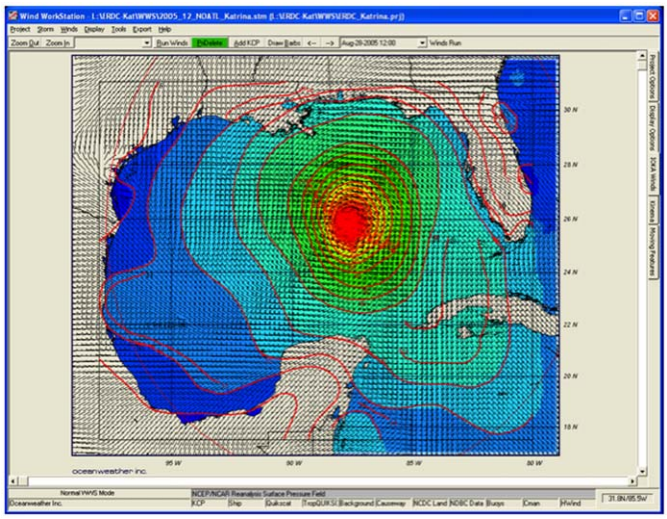

Fig. 15. WWS display valid for 28 August 2005 at 12:00 GMT showing blended wind field.

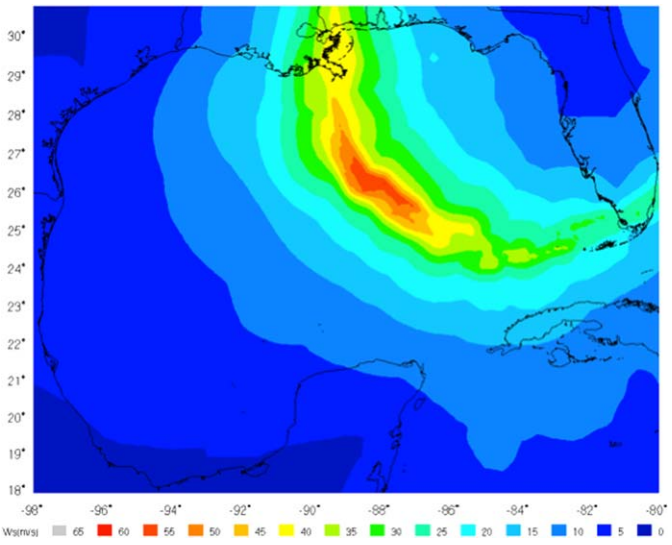

Fig. 16. Maximum 30 min wind speed (m/s) on basin grid.

6. Summary and conclusion

An analysis of record has been assembled for Hurricane Katrina's surface wind distribution at a 3 h frequency from its emergence into the Gulf of Mexico through landfall. A comprehensive set of surface wind measurements from marine- (buoys, ships, platforms), land- (portable mesonet stations, aviation, and agriclimate weather stations, Doppler radar), space- (scatterometers and cloud drift winds), and aircraft-based platforms (flight-level hurricane reconnaissance aircraft, GPS sondes, SFMR, and Doppler radar) were assembled, standardized, and quality controlled using the H*Wind system. The resulting data were objectively analyzed and gridded and are available at (www.aoml.noaa.gov/hrd/Storm_pages/katrina2005/wind.html). The H*Wind gridded fields were then blended with peripheral data, adjusted to a 30 min averaging period representative of ocean response to winds, and interpolated to 15 min storm track time step using the IOKA system. The final wind field grid was then interpolated to the grids used for the storm surge (ADCIRC) and wave models (WAM, Wave Watch, SDWave). Despite a decrease in Hurricane Katrina's intensity from a Saffir–Simpson Category 5 (when near a warm-core ocean eddy) down to Category 3 during the 24 h period leading up to landfall, an expansion of the wind field caused Katrina to approximately conserve integrated kinetic energy, with a value for winds > tropical storm-force twice as large as Hurricane Camille of 1969.

Table 3
Wind statistics at select NDBC buoy locations.

	Station	Number of Pts	Mean meas	Mean hind	Diff (H-M)	RMS error	Stnd dev	Scat index	Corr coeff
Wind spd. (m/s)	42001	145	9.26	9.50	0.23	1.34	1.32	0.14	0.98
Wind dir. (deg)	42001	145	0.41	342.78	4.57	N/A	13.70	0.04	N/A
Wind spd. (m/s)	42003	78	12.73	11.62	−1.11	1.88	1.51	0.12	0.99
Wind dir. (deg)	42003	78	41.17	31.47	−9.33	N/A	11.88	0.03	N/A
Wind spd. (m/s)	42007	103	7.80	6.98	−0.82	1.74	1.54	0.20	0.94
Wind dir. (deg)	42007	103	86.99	75.45	−12.08	N/A	21.66	0.06	N/A
Wind spd. (m/s)	42040	145	10.74	11.03	0.29	1.09	1.05	0.10	0.99
Wind dir. (deg)	42040	145	86.75	83.22	3.02	N/A	18.20	0.05	N/A
Wind spd. (m/s)	42067	107	8.24	8.14	−0.10	1.40	1.40	0.17	0.97
Wind dir. (deg)	42067	107	82.42	77.17	−5.32	N/A	22.39	0.06	N/A

Acknowledgements

The authors appreciate the cooperation of many scientists, data managers, and programs in providing observation data sets to help supplement our investigation. In particular we thank: Peter Black of SAIC, Rick Knabb (formerly of the National Hurricane Center), Forrest Masters and Kurt Gurley of the University of Florida, John Schroeder and Ian Giammanco of Texas Tech University, Robert Howard of Lousiana State University (LSU), Stephan Howden of University of Southern Mississippi, David Gilhousen (formerly of NOAA National Data Buoy Center), Frank Revitte of the New Orleans National Weather Service Forecast Office, Paul Chang of the NOAA National Environmental Satellite and Data Information Service, Royce Fontenot of the Louisiana, Mississippi and Alabama Agriclimatic Network, Systke Kimball and Keith Blackwell of the University of South Alabama, James Finney, Chris Turner of the Federal Aviation Administration, William Henderson and Glen Argabright of the NASA Michoud Assembly Facility, The Louisiana Universities Marine Consortium, The National Estuary Program, the Wave and Current Information System at LSU, and the Pearl River and Jackson County Emergency Operations Centers. We appreciate the helpful comments from the anonymous reviewers. This study was support by the Interagency Performance Evaluation Task Force through the US Army Corps of Engineers.

References

Black, P., 1994. Evolution of maximum wind estimates in typhoons. In: Lighthill, J.L., Zhemin, Z., Holland, G., Emmanuel, K. (Eds.), Tropical Cyclone Disasters. Peking University Press, China, pp. 104–115.

Cardone, V.J., Jensen, R.E., Resio, D.T., Swail, V.R., Cox, A.T., 1996. Evaluation of contemporary ocean wave models in rare extreme events: Halloween storm of October, 1991; Storm of the century of March, 1993. J. Atmos. Oceanic Technol. 13, 198–230.

Cox, A.T., Greenwood, J.A., Cardone, V.J., Swail, V.R., 1995. An interactive objective kinematic analysis system. Proceedings 4th International Workshop on Wave Hindcasting and Forecasting, October 16–20, 1995, Banff, Alberta, p. 109–118. Available from Environment Canada, Downsview, Ontario.

Cline, I.M., 1920. Relation of changes in storm tides on the coast of the Gulf of Mexico to the center and movement of hurricanes. Mon. Wea. Rev. 48, 127-146.

Dunion, J.P., Houston, S.H., Velden, C.S., Powell, M.D., 2002. Application of surface-adjusted GOES low-level cloud-drift winds in the environment of Atlantic tropical cyclones. Part II: integration into surface wind analyses. Mon. Weather Rev. 130, 1347–1355.

Engineering Sciences Data Unit (ESDU), 1982. Strong winds in the atmospheric boundary layer, Part 1: Mean hourly wind speed. Item no. 82026, 63 pp.

Franklin, J.L., Black, M.L., Valde, K., 2003. GPS dropwindsonde wind profiles in hurricanes and their operational implications. Weather Forecast. 18, 32–44.

Gamache, J.F., Marks, F.D., Roux, F., 1995. Comparison of three airborne Doppler sampling techniques with airborne in situ wind observations in Hurricane Gustav (1990). J. Atmos. Oceanic Technol. 12, 171–181.

Hock, T.R., Franklin, J.L., 1999. The NCAR GPS dropwindsonde. Bull. Am. Meteorol. Soc. 80, 407–420.

Houze, R., 2007. Hurricanes can form new eyewall and change intensity rapidly. ScienceDaily, Mar. 7. www.sciencedaily.com.

Howden, S., Gilhousen, D., Guinasso, N., Alpert, J., Sturgeon, M., Bender, L., 2008. Hurricane Katrina winds measured by a buoy-mounted sonic anemometer. J. Atmos. Oceanic Technol. 25, 607–616.

Lee, W.-C., Jou, B.J.-D., Chang, P.-L., Deng, S.-M., 1999. Tropical cyclone kinematic structure retrieved from single Doppler radar observations. Part I. Interpretation of Doppler velocity patterns and the GBVTD technique. Mon. Weather Rev. 127, 2419–2439.

Liu, W.T., Katsaros, K.B., Businger, J.A., 1979. Bulk parameterizations of air-sea exchanges of heat and heat and water vapor including the molecular constants at the surface. J. Atmos. Sci. 36, 1722–1735.

Mc Taggart-Cowan, R., Bosart, L.F., Gyakum, J.R., Atallah, E.H., 2007. Hurricane Katrina (2005). Part I: complex life cycle of an intense tropical cyclone. Mon. Weather Rev. 135, 3905–3926.

Persing, J., Montgomery, M.T., 2003. Hurricane superintensity. J. Atmos. Sci. 60, 2349–2371.

Powell, M.D., Houston, S.H., Reinhold, T.A., 1996. Hurricane Andrew's landfall in South Florida. Part I: standardizing measurements for documentation of surface wind fields. Weather Forecast. 11, 304–328.

Powell, M.D., Houston, S.H., 1996. Hurricane Andrew's landfall in South Florida. Part II: surface wind fields and potential real-time applications. Weather Forecast. 11, 329–349.

Powell, M.D., Houston, S.H., Amat, L.R., Morisseau-Leroy, N., 1998. The HRD real-time surface wind analysis system. J. Wind Eng. Ind. Aerodyn. 77–78, 53–64.

Powell, M.D., Vickery, P.J., Reinhold, T.A., 2003. Reduced drag-coefficient for high wind speeds in tropical cyclones. Nature 422, 279–283.

Powell, M.D., Bowman, D., Gilhousen, D., Murillo, S., Carrasco, N., St. Fleur, R., 2004. Tropical cyclone winds at landfall: the ASOS-CMAN wind exposure documentation project. Bull. Am. Meteorol. Soc. 85, 845–851.

Powell, M.D., Reinhold, T.A., 2007. Tropical cyclone destructive potential by integrated kinetic energy. Bull. Am. Meteorol. Soc. 87, 513–526.

Powell, M.D., Uhlhorn, E.W., Kepert, J., 2009. Estimating Maximum Surface Winds from Hurricane Reconnaissance Measurements. Weather Forecasting, 24, 868-883.

Quilfen, Y., et al., 2007. The potential of QuikSCAT and WindSat observations for the estimation of sea surface wind vector under severe weather conditions. J. Geophys. Res. 112, C09023.

Shay, L.N. Air–Sea Interactions. Global Perspectives of Tropical Cyclones. Ed. J. Chan, World Meteorological Organization, in press.

Simiu, E., Scanlan, R., 1996. Wind Effects on Structures. Wiley Interscience 704 pp.

Uhlhorn, E.W., Black, P.G., 2003. Verification of remotely sensed sea surface winds in hurricanes. J. Atmos. Oceanic Technol. 20, 99–116.

Uhlhorn, E.W., Black, P.G., Franklin, J.L., Goodberlet, M., Carswell, J., Goldstein, A.S., 2007. Hurricane surface wind measurements from an operational stepped frequency microwave radiometer. Mon. Weather Rev. 135, 3070–3085.

Vickery, P.J., Skerlj, P.F., 2005. Hurricane gust factors revisited. J. Struct. Eng. 131, 825–832.

Vickery, P.J., Wadhera, D., Powell, M.D., Chen, Y., 2009. Hurricane boundary layer and wind field model for use in engineering applications. J. Appl. Meteorol Climate 48, 381–405.

Weiringa, J., 1992. Updating the Davenport roughness classification. J. Wind Eng. 41, 357–368.

Willoughby, H.E., Clos, J.A., Shoreibah, M.G., 1982. Concentric eyewalls, secondary wind maxima, and the evolution of the hurricane vortex. J. Atmos. Sci. 39, 395–411.

Wimmers, A. J., Velden, C.S., 2007. MIMIC: A new approach to visualizing satellite microwave imagery of tropical cyclones. Bull. Am. Meteorol. Soc. 88, 1187-1196.